Chinese Journal of Structural Chemistry 44 (2025) 100504

Contents lists available at ScienceDirect

Chinese Journal of Structural Chemistry

journal homepage: www.journals.elsevier.com/chinese-journal-of-structural-chemistry

Article

# Break the capacity limit of $Li_4Ti_5O_{12}$ anodes through oxygen vacancy engineering

Jianjun Fang [a,b,d,1], Kunchen Xie [a,1], Yongli Song [c,***], Kangyi Zhang [d], Fei Xu [d], Xiaoze Shi [e], Ming Ren [d], Minzhi Zhan [a], Hai Lin [a,b], Luyi Yang [a], Shunning Li [a,**], Feng Pan [a,*]

[a] School of Advanced Materials, Peking University Shenzhen Graduate School, Shenzhen, 518055, PR China
[b] Weiming Battery Technology Co., Ltd, Guangdong, PR China
[c] School of Energy and Power Engineering, Jiangsu University, Zhenjiang, 212013, PR China
[d] Qiantu Battery Technology Co., Ltd, Guangdong, PR China
[e] BAK Power Battery Co., Ltd., Guangdong, PR China

ARTICLE INFO

*Keywords:*
$Li_4Ti_5O_{12}$
Oxygen vacancies
Anode
Excess capacity

ABSTRACT

The zero-strain spinel $Li_4Ti_5O_{12}$ stands out as a promising anode material for lithium-ion batteries due to its outstanding cycling stability. However, the limited theoretic specific capacity, low $Li^+$ diffusion coefficient and electronic conductivity severely hinder its practical application. In this study, we demonstrate a strategy of introducing abundant oxygen vacancies not only on the surface and but also inside the bulk of $Li_4Ti_5O_{12}$ particles via reductive thermal sintering. The oxygen vacancies can significantly enhance the electronic conductivity and lithium-ion diffusion coefficient of $Li_4Ti_5O_{12}$, leading to a remarkable improvement in rate performance and a reduction in polarization. Moreover, additional lithium-ion accommodation sites can be created at the defective surface, contributing to a high specific capacity of over 200 mAh $g^{-1}$.

## 1. Introduction

In recent years, lithium-ion batteries have seen widespread use in various electronic devices, including mobile phones, laptops, electric bicycles, and electric vehicles. This popularity is due to their numerous advantages, such as high operating voltage, high energy density, memory-free characteristics, and long cycle life [1,2]. Currently, graphite and its derivatives are the most commonly used materials for negative electrodes [3]. However, these carbon materials are prone to reacting with the electrolyte to form a solid electrode/electrolyte interface (SEI) film during operation, resulting in the loss of active lithium ions in the electrolyte [4]. Furthermore, the repeated intercalation and deintercalation of lithium ions deteriorate the structures of carbon materials, causing significant degradation. The growth of lithium dendrites can also cause short circuits in batteries, posing safety hazards such as fire and even explosion during high-power pulse charging [5,6]. Therefore, there is an increasing need to discover new negative electrode materials that are safe, reliable, and offer higher specific capacity and longer cycle life.

Compared to carbon anodes, spinel lithium titanate is seen as a promising anode material for lithium-ion batteries because of its excellent structural stability and good cycle life. It is particularly suitable for large-scale energy storage applications [7]. Lithium titanate $Li_4Ti_5O_{12}$ (LTO) is known as a "zero strain material" due to its negligible volumetric change during lithium-ion intercalation and deintercalation, resulting in excellent cycling performance [8–10]. LTO also possesses excellent safety characteristics and relatively higher intercalation potential (1.55 V *vs.* $Li/Li^+$) of lithium ions during the discharge process, helping to prevent the lithium dendrites and SEI formation [11], also helpful for the application of LTO in aqueous batteries [12]. However, its low electronic conductivity ($< 10^{-13}$ S $cm^{-1}$) and limited $Li^+$ diffusion coefficient severely restrict the high-rate performance of LTO, hindering the full utilization of its theoretical capacity (175 mAh $g^{-1}$) [13–16].

To address these drawbacks, numerous studies have been conducted on the doping of elements such as Cr, W, Na, and V, as well as carbon coating, to modify the LTO structure, resulting in significant progress [17–21]. Recent research has shown that introducing oxygen vacancies can effectively

* Corresponding author.
** Corresponding author.
*** Corresponding author.
*E-mail addresses:* songyl@ujs.edu.cn (Y. Song), lisn@pku.edu.cn (S. Li), panfeng@pkusz.edu.cn (F. Pan).
[1] J. Fan and K. Xie contributed equally to this work.

https://doi.org/10.1016/j.cjsc.2024.100504
Received 25 October 2024; Received in revised form 1 December 2024; Accepted 5 December 2024
Available online 13 January 2025

enhance the electrochemical properties and cycling performance of LTO materials. The existence of oxygen vacancies narrows the bandgap, thereby improving the electronic conductivity of LTO and enhancing the diffusion kinetics of lithium ions. As a result, LTO materials with higher energy density and improved rate performance have been achieved [22–27].

Here, through thermal reduction, we reconstruct the spinel LTO structure with substantial oxygen vacancies. The introduced oxygen vacancies distributed both on the surface and within the bulk of LTO particles greatly promote the charge transfer within the LTO particles, resulting in excellent rate performance. Furthermore, the rapid transmission of lithium ions and electrons mitigates polarization, allowing the theoretical capacity (175 mAh $g^{-1}$) of LTO to be fully realized. Consequently, the as-prepared LTO negative electrode material exhibits an ultra-high specific capacity of over 200 mAh $g^{-1}$ and stable cycling performance under 5 C. The demonstrated structural reconstruction strategy to regulate lithium-ion diffusion and storage open up new directions for the advancement of industrial applications of LTO materials.

## 2. Results and discussion

The only difference between $Li_4Ti_5O_{12}$ (P-LTO) and $Li_4Ti_5O_{12-x}$ (OV-LTO) during the synthesis process is the sintering atmospheric conditions, with P-LTO synthesized in an argon atmosphere while OV-LTO in an $Ar/H_2$ mixture reductive atmosphere. The $H_2$ atmosphere induces the generation of oxygen vacancies, leading to the formation of color center orbitals in the oxide. These color center orbitals readily capture photons, resulting in a darker color of OV-LTO [28,29]. Fig. S1 demonstrates the different colors of P-LTO (white) and OV-LTO (blue), indicating a higher concentration of oxygen vacancies in OV-LTO. Scanning electron microscopy (SEM) images of P-LTO and OV-LTO are displayed in Figs. S2 and 1(a), respectively. The morphology and particle size of both materials are similar (~1 μm). X-ray diffraction (XRD) data in Fig. S3 confirm that P-LTO and OV-LTO are pure phases without heterophase like $TiO_2$, which could affect capacity [30–32]. Fig. 1(b) provides the XRD patterns for the (111) lattice planes of P-LTO and OV-LTO. The introduction of oxygen vacancies in OV-LTO leads to a significant presence of $Ti^{3+}$, causing lattice expansion and a shift in the diffraction peak towards a smaller angle [22,33]. This suggests that the oxygen vacancies in OV-LTO are distributed throughout the entire particle, considering the detection depth of XRD. High-resolution transmission electron microscopy (HRTEM) data for P-LTO and OV-LTO are shown in Figs. 1(d) and S4, respectively. Further analysis (Fig. S5) reveals that the (111) lattice plane distances of P-LTO and OV-LTO are 0.481 and 0.485 nm, respectively, consistent with the XRD data. Electron paramagnetic resonance (EPR) was utilized to characterize the presence of oxygen vacancies (Fig. 1(c)). The g-factor ($g = 2.08$) for both P-LTO and OV-LTO can be determined from the EPR results, indicating the presence of unpaired electrons captured by oxygen vacancies [24,34]. It is worth noting that P-LTO also shows a signal at $g = 2.08$, which may be attributed to trace oxygen vacancies on the surface of P-LTO. It should be pointed out that compared to the work of Huang and Chen, the OV-LTO signal in our work is more pronounced, indicating that the OV-LTO has a higher concentration of oxygen vacancies [22,24]. Combining XRD and TEM results, it can be inferred that the high concentration of oxygen vacancies is attributed to the oxygen vacancies in the LTO bulk phase. The Raman data corroborate the EPR results, showing a blueshift of the peak at 150 $cm^{-1}$, which implies the reduction of $Ti^{4+}$ (Fig. S6) [23,24]. X-ray photoelectron spectroscopy (XPS) data in Fig. 1(e) show that Ti ions in P-LTO exist as $Ti^{4+}$, suggesting negligible oxygen vacancy content. This is consistent with the XPS data for O in P-LTO shown in Fig. S7(a). In contrast, OV-LTO exhibits a significant amount of $Ti^{3+}$ (Fig. 1(f)) and oxygen vacancies (Fig. S7(b)). The oxygen vacancy concentration was determined to be $4.65 \times 10^{21}$ vacancies $cm^3$ by comparing the peak areas of $Ti^{3+}$ and $Ti^{4+}$, which corresponds to approximately 10.2% of the total oxygen atoms being vacant. In conclusion, we successfully introduced rich oxygen vacancies both on the surface and within the bulk of OV-LTO material by utilizing the $Ar/H_2$ sintering environment, without generating any impurities or affecting particle size and morphology.

To further verify the electrochemical characteristics of P-LTO and OV-LTO, coin cells were assembled with as-prepared electrode material, and the galvanostatic charge/discharge profiles were analyzed. Measurements were conducted at a current density of 0.1 C between a voltage range of 1.0–3.0 V, as shown in Fig. 2(a and b). Both P-LTO and OV-LTO exhibit a pair of distinct charge and discharge plateaus around 1.55 V, corresponding to the $Li^+$ intercalation and deintercalation process in LTO as follows:

$$Li_4Ti_5O_{12} + 3Li^+ + 3e^- = Li_7Ti_5O_{12} \quad (1)$$

Notably, the potential gap between the charge and discharge plateaus for the OV-LTO electrode is 100 mV, smaller than that of P-LTO (130 mV),

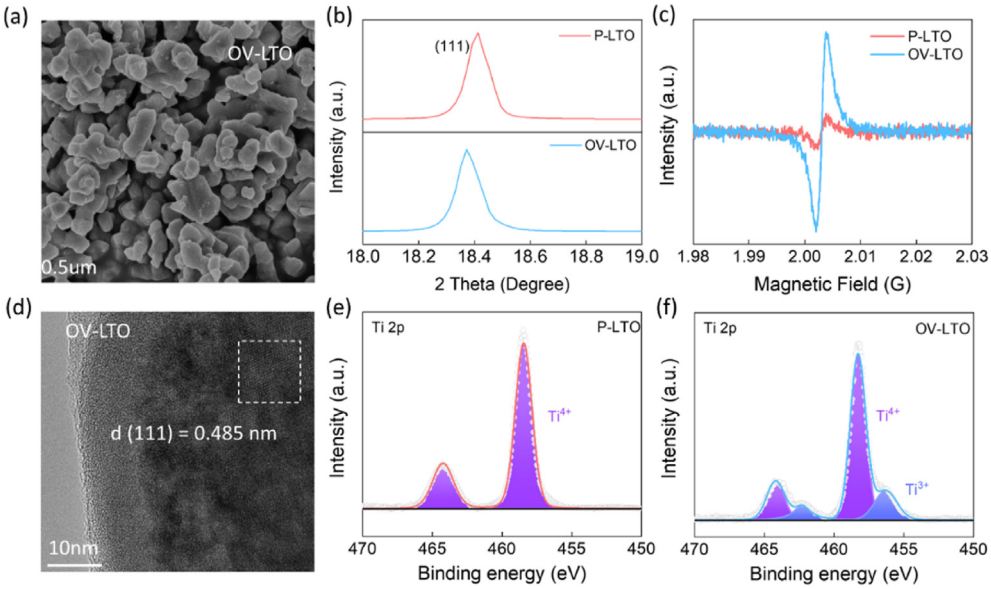


**Fig. 1.** (a) SEM observation of OV-LTO. (b) XRD patterns of the (111) lattice planes for P-LTO and OV-LTO. (c) EPR spectra of P-LTO and OV-LTO. (d) HRTEM of OV-LTO. (e) XPS core spectra of Ti 2p for P-LTO and (f) XPS core spectra of Ti 2p for OV-LTO.

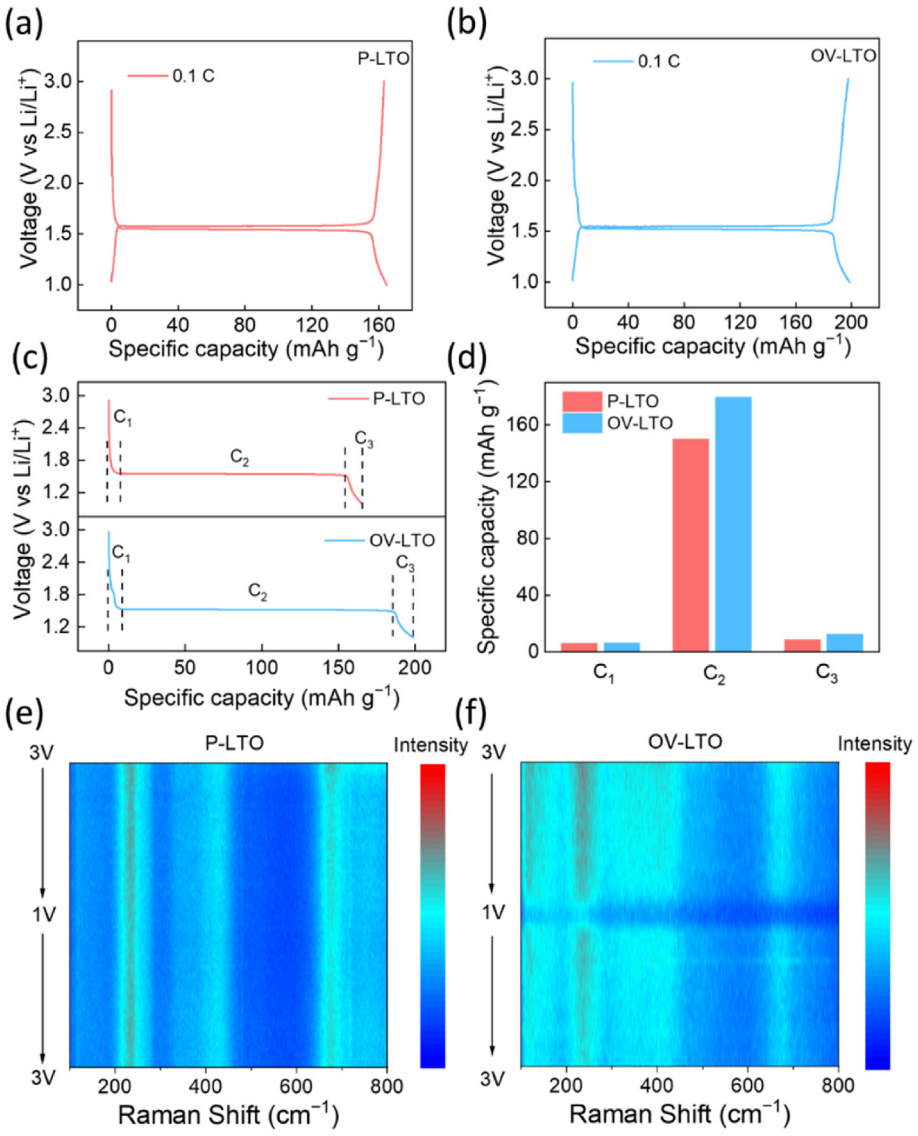


**Fig. 2.** The typical voltage curves at 0.1 C rate of (a) P-LTO and (b) OV-LTO. (c) Charge curves of P-LTO and OV-LTO at 0.1 C. (d) The corresponding capacity contribution of different phases for P-LTO and OV-LTO. *In-situ* Raman spectroscopy observation of (e) P-LTO and (f) OV-LTO during cycling.

indicating facilitated reaction kinetics of OV-LTO due to the generation of oxygen vacancies. In Fig. 2(c), we compare the discharge profiles of P-LTO and OV-LTO at 0.1 C. Three typical stages can be identified including: $C_1$, from the open-circuit potential to ~1.55 V, corresponding to the intercalation of $Li^+$ into the LTO solid solution; $C_2$, the discharge plateau at ~1.55 V, involving the dual-phase transformation of $Li_4Ti_5O_{12}$ to $Li_7Ti_5O_{12}$; and $C_3$, the potential region from ~1.55 to 1 V, related to $Li^+$ storage at the solid-liquid and solid-solid interfaces [24]. In general, the lithium-ion interaction during $C_2$ dominates the intrinsic capacity of LTO, while $C_1$ and $C_3$ represent pseudocapacitive behaviors. The presence of this pseudocapacitance has resulted in reports of LTO demonstrating capacities that reach or even exceed its theoretical capacity (175 mAh $g^{-1}$) [35]. Fig. 2(d) shows that the certified capacity density of P-LTO (corresponding to the $C_2$ part) is 150 mAh $g^{-1}$, much lower than the theoretical specific capacity of LTO owing to sluggish electron and $Li^+$ ion transport. The generation of abundant oxygen vacancies in OV-LTO facilitates the rapid transfer of electrons and $Li^+$ ions, resulting in an enhanced intrinsic capacity of 174.6 mAh $g^{-1}$. The $C_1$ capacity of both P-LTO and OV-LTO is nearly identical, indicating the absence of impurities such as $TiO_2$, which could otherwise increase the material's capacity density [30–32]. Additionally, the $C_3$ capacity of OV-LTO is 13.6 mAh $g^{-1}$, higher than that of P-LTO (9.8 mAh $g^{-1}$), indicating the increase in accommodation sites of $Li^+$ ion at the defective surface [36–38]. To reveal the surface structural evolution of the LTO anode during cycling, *in-situ* Raman spectra (Fig. 2(e and f)) were conducted. Three typical peaks centered at ~233, 429 and 675 $cm^{-1}$, corresponding to the characteristic $F_{2g}$, $E_g$ and $A_{1g}$ modes of Ti–O vibrations, respectively. During cycling, all peaks disappear in OV-LTO at low voltages, suggesting the destabilization of Ti–O bonds because of the adsorption of lithium ions in oxygen vacancies [39]. To further explore the mechanism by which oxygen vacancies enhance the capacity of OV-LTO, we calculated the oxygen vacancy formation energy ($E_{vac}$) for the two distinct oxygen sites in $Li_4Ti_5O_{12}$ and the voltage plateau associated with lithium extraction from the lattice (U) (Fig. S9). The theoretical calculations, combined with *in-situ* Raman spectroscopy results, reveal that the presence of oxygen vacancies induces partial reduction of Ti to the +3 oxidation state. This not only facilitates the further extraction of lattice lithium, but also enhances the electronic conductivity by modifying the electronic structure of OV-LTO. Moreover, oxygen vacancies provide more efficient diffusion pathways for lithium ions by reducing the interaction between oxygen ions, thereby improving the overall ion mobility. In summary, the introduction of abundant oxygen vacancies in LTO not only fully demonstrates the intrinsic capacity of LTO

but also provides some additional capacity density through the adsorption of lithium ions by oxygen vacancies. Combined with the existing pseudocapacitance effect, the capacity density of OV-LTO reaches 198.6 mAh $g^{-1}$.

The rate performance of P-LTO and OV-LTO at current densities ranging from 0.1 to 10 C is shown in Fig. 3(a). It can be observed that the average discharge capacity of OV-LTO is 198 mAh $g^{-1}$ at 0.1 C, significantly higher than that of P-LTO (162 mAh $g^{-1}$). At high current densities, the capacity of P-LTO shows a substantial drop, reaching only 108 mAh $g^{-1}$ at 10 C, while OV-LTO maintains a much higher capacity of 151 mAh $g^{-1}$. Moreover, after 30 cycles under different C-rates, the discharge capacity returns to the capacity of the initial cycle when the rate returns to 0.1 C. Compared with other reports on LTO materials, the OV-LTO in our work not only exhibits ultra-high capacity but also demonstrates excellent rate performance, as shown in Fig. 3(b) [17,40–45]. Fig. 3(c and d) displays the voltage-capacity curves at various rates from 0.1 to 10 C for P-LTO and OV-LTO. OV-LTO exhibits higher reversible specific capacity and capacity retention (compared to the capacity at 0.1 C) at every current density than P-LTO, indicating its outstanding rate performance. Additionally, OV-LTO shows much smaller polarization at high C-rates compared to P-LTO. The excellent rate performance of OV-LTO can be attributed to the improved conductivity and reduced charge transfer resistance, as shown in the EIS spectra (Fig. S8). The presence of oxygen vacancies in OV-LTO enhances electron conductivity, which stems from the narrowed bandgap, consequently resulting in lower polarization and excellent capacity at high C-rates. Moreover, the introduced oxygen vacancies also increase the migration ability of lithium ions. The improvement of the electronic conductivity of materials due to oxygen vacancies has been demonstrated in many reports from both theoretical and experimental perspectives [46–48]. For example, Mai et al. demonstrated that introducing oxygen vacancies would enhance the electrical conductivity as well as facilitate the ion diffusion of anatase $TiO_2$ [49].

The $Li^+$-ion diffusion coefficients of P-LTO and OV-LTO were determined using the CV technique [41]. The P-LTO/Li and OV-LTO/Li cells were tested at a scan rate of 0.1 mV $s^{-1}$ for the first cycle, and then successively at 0.2, 0.4, 1.0, 2.0 and 4.0 mV $s^{-1}$ for one cycle each (Fig. 4(a and d)). The relationship between the oxidation peak currents ($I_p$) and the square root of scan rate ($\nu^{0.5}$) was numerically linear, as shown in Fig. 4(b and e). Consequently, the $Li^+$-ion diffusion coefficient ($D_{Li}$) can be confirmed using the Randles-Sevcik equation as follows:

$$I_p = 0.4463 n^{1.5} F^{1.5} C_{Li} S R^{-0.5} T^{-0.5} D_{Li}^{0.5} \nu^{0.5} \quad (2)$$

where $n$ refers to the number of electrons transferred during the electrochemical reaction, and $F$, $C_{Li}$, $S$, $R$ and $T$ represent the Faraday's constant, $Li^+$ concentration, contact area between the active material and electrolyte, molar gas constant, and absolute temperature, respectively [50]. The $Li^+$ diffusion coefficients of P-LTO and OV-LTO are $5.48 \times 10^{-8}$ and $1.24 \times 10^{-7}$ $cm^2$ $s^{-1}$, indicating that introducing oxygen vacancies facilitates faster lithium ion transport in LTO.

The relationship between peak current ($i$) and scan rate ($v$) could be calculated using the equation $i = av^b$ [51,52], which can be transformed as follows:

$$\log(i) = b\log(v) + \log(a) \quad (3)$$

where the value of $b$ is always between 0.5 and 1, associated with the electron storage characteristics of the electrochemical reaction. Specifically, a smaller $b$ indicates that the ionic diffusion controls the electrochemical reaction, whereas a larger $b$ suggests the faradaic reaction to be dominant [24]. The calculated $b$ values for the oxidation and reduction processes of P-LTO are 0.526 and 0.501 (Fig. 4(c)), respectively, implying that ionic diffusion dominates the electrochemical process of P-LTO. Inversely, the corresponding values of $b$ for OV-LTO shown in Fig. 4(f) are 0.588 and 0.527, respectively, revealing the additional faradaic reactions in OV-LTO, generated from the introduced oxygen vacancies. This is consistent with the results shown in Fig. 2(d).

The cycle performance of P-LTO and OV-LTO at different C-rates is shown in Fig. 5. The capacity of OV-LTO is significantly higher than that of P-LTO at all three C-rates, which aligns with the cycle performance data presented in Fig. 3(a). Specifically, the specific capacity of OV-LTO is 193 mAh $g^{-1}$ after 100 cycles at a discharge current density of 0.1 C, with a capacity retention of 95%. In contrast, after the same number of

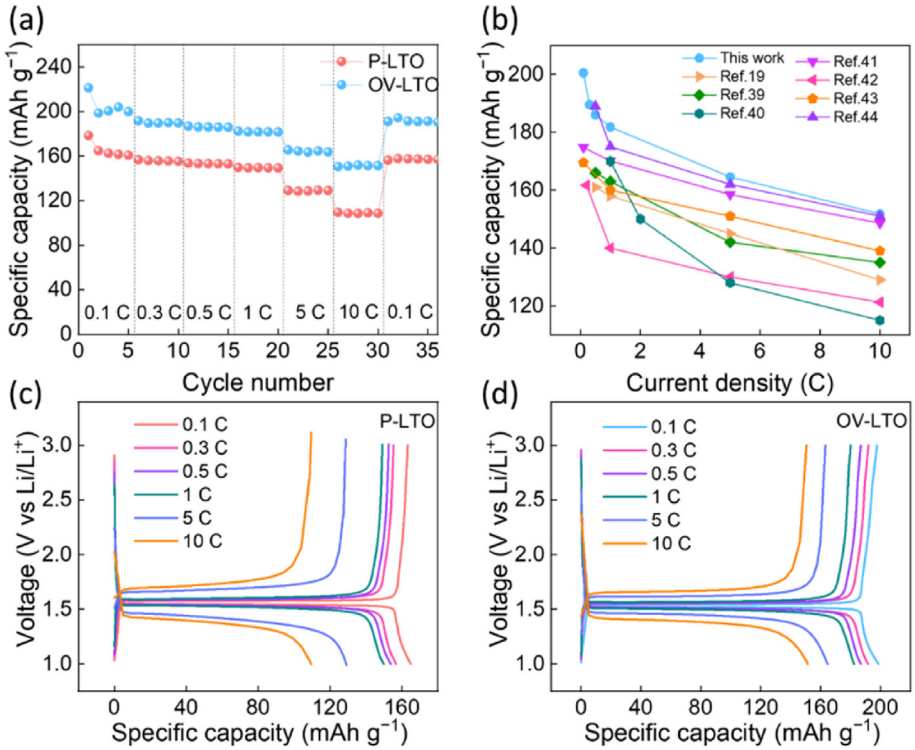


**Fig. 3.** (a) Cycle performance of P-LTO and OV-LTO. (b) Comparison of capacity at various rates. Rate performances of P-LTO (c) and OV-LTO (d).

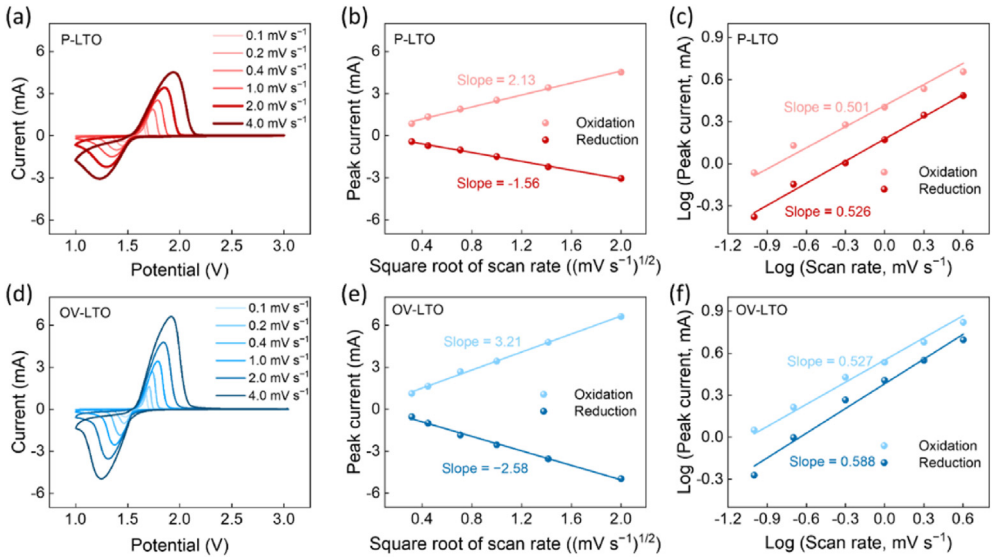


**Fig. 4.** CV curve under various scanning rates of (a) P-LTO and (d) OV-LTO. The linear relationship between the peak current ($I_p$) of the oxidation/reduction process and the square root of scan rate ($\nu^{0.5}$) for (b) P-LTO and (e) OV-LTO. The linear relationship between the peak current ($I_p$) of oxidation/reduction process and scan rate ($\nu$) for (c) P-LTO and (f) OV-LTO.

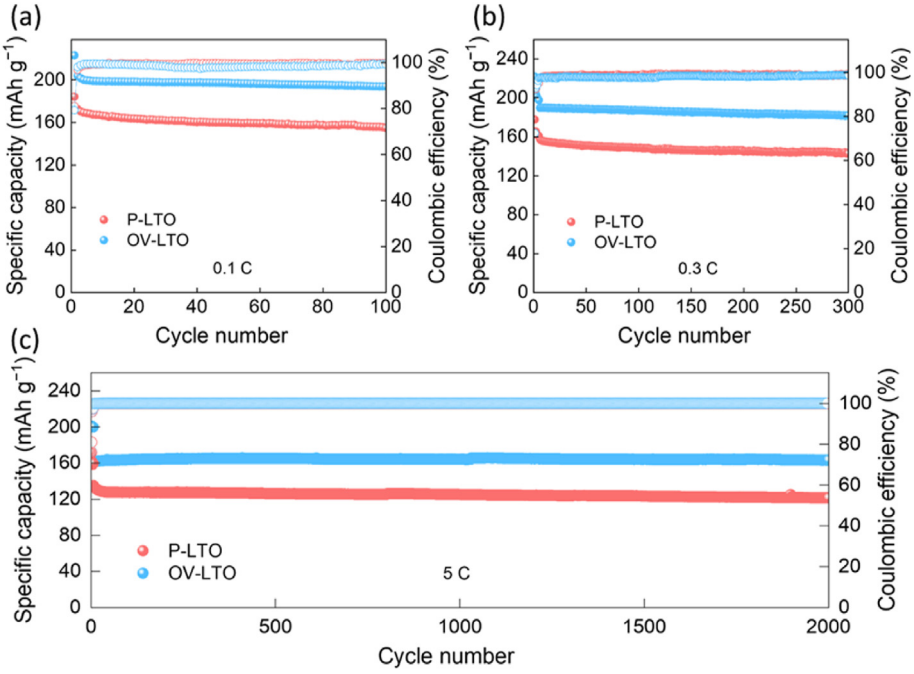


**Fig. 5.** Cycling performance of P-LTO and OV-LTO at (a) 0.1 C, (b) 0.3 C and (c) 5 C.

cycles the capacity and retention rate of P-LTO are only 154 mAh $g^{-1}$ and 89%, respectively (Fig. 5(a)). OV-LTO also exhibits high capacity retention of 95% at 0.3 C (Fig. 5(b)). Fig. 5(c) demonstrates even at a discharge rate of 5 C, OV-LTO maintains a discharge capacity of 163 mAh $g^{-1}$ and retains 98% of its initial discharge capacity over 2000 cycles, significantly higher than that of P-LTO (121 mAh $g^{-1}$, 89%). Besides, under high mass loading conditions (9.4 mg $cm^{-2}$), although the capacity of OV-LTO showed a slight decrease, the overall performance remained consistent with the results obtained at lower loadings (2 mg $cm^{-2}$) (Fig. S10). To further verify the practical application potential of OV-LTO, we compared the cycling performance of Lithium cobalt oxide (LCO)||P-LTO and LCO||OV-LTO full batteries in the voltage range of 1.5–3.1 V. As shown in Fig. S11, the full battery using OV-LTO demonstrates higher cycling stability than that using P-LTO, indicating that OV-LTO is well-suited for common cathode materials such as LCO. Overall, the introduction of oxygen vacancies has greatly enhanced the capacity density, rate performance, and long-cycle stability of OV-LTO by improving the transport capabilities of electrons and lithium ions within LTO.

## 3. Conclusion

In summary, a lithium titanate anode material with a high concentration of oxygen vacancies was prepared by sintering in an Ar/$H_2$ atmosphere. The introduction of oxygen vacancies significantly enhances the electrochemical performance of OV-LTO, including its $Li^+$ ion

diffusion coefficient and electron transfer ability. As a result, OV-LTO exhibits excellent cycling and rate performance. Moreover, charge transfer efficiency is promoted, which reduces the polarization and allows for the full release of the theoretical capacity of LTO bulk phase. Moreover, oxygen vacancies can provide additional capacity by creating additional accommodation sites for lithium ions, leading to an ultra-high capacity of ~200 mAh $g^{-1}$. The proposed structural reconstruction strategy shows great potential for manipulating lithium-ion diffusion and developing high-power density anode materials in lithium-ion batteries.

## 4. Experimental

### 4.1. Preparation of $Li_4Ti_5O_{12}$ and $Li_4Ti_5O_{12-x}$

Both P-LTO and OV-LTO were prepared using the solid-phase method. Firstly, titanium dioxide and lithium carbonate were weighed according to the stoichiometric ratio of LTO, and then mixed homogeneously by ball milling to obtain the precursor. The precursor was then placed in a porcelain boat and heated to 800 °C in a tube furnace for 6 h, after which it was naturally cooled to room temperature to obtain the target substances. The heating rate is 10 °C per minute. The calcination atmosphere is argon for P-LTO and argon/hydrogen mixture (95:5 vol%) for OV-LTO. The final products were stored in an argon-filled glove box for storage to prevent natural oxidation in the air.

### 4.2. Materials characterization

XRD (Bruker D8 Advance diffractometer) was used to characterize the phase and structural information of the as-prepared powders. Morphologies were verified by SEM (ZEISS Supra 55). XPS (ESCALAB 250Xi spectrometer) with Al K$\alpha$ radiation was used to characterize the valent state of Ti and the potential existence of oxygen vacancies. All XPS spectra were calibrated based on the C 1s photoelectron peak at 284.8 eV as the reference. The wavelength of the argon laser in the Raman spectrometer (Renishaw InVia) experiment was 532 nm. HRTEM images were collected using JEOL3200FS field-emission transmission electron microscopy (FETEM). The focused ion beam (FIB, FEI, Scios) was used to obtain cross-section samples. EPR (Bruker A300-10/12) was conducted to measure oxygen vacancies in LTO.

### 4.3. Electrochemical measurements

The CR2032 coin-type half cells were assembled to characterize the electrochemical performance of the materials with Li foil as the reference electrode. The electrolyte consisted of 1.2 M $LiPF_6$ in ethylene carbonate (EC) and diethylene carbonate (DEC) (1:1 vol%) with 10 vol% fluoroethylene carbonate (FEC). The cathode slurry contained 80 wt% cathode materials, 10 wt% super P carbon black and 10 wt% polyvinylidene fluoride (PVDF) binder. Cathode electrodes were prepared by coating the slurry onto Cu foil and then drying it overnight at 80 °C in a vacuum oven to prevent oxidation, with an average sample mass loading of about 2 mg $cm^{-2}$. The cycling tests were carried out using a Neware battery test system with a voltage range of 1–3 V (*vs.* $Li/Li^+$) for anodes. Cyclic voltammetry (CV) curves were collected on a CHI 660E electrochemical workstation with a scan rate ranging from 0.1 to 4 mV $s^{-1}$ between 1 and 3 V. The resistivity of electrodes was calculated from data collected by the CHI 660E electrochemical workstation in the frequency range from 1 MHz to 1 Hz with 5 mV amplitude at room temperature.

### 4.4. Theoretical calculation

All spin-polarized density functional calculations were performed with the projector-augmented wave (PAW) method and Perdew-Burke-Ernzerhof (PBE) exchange correlation potential by Vienna *ab initio* simulation package (VASP). The plane-wave energy cutoff was set as 520 eV and the criterion for electronic energy convergence and forces in geometry optimization was set to 10–5 eV and 0.02 eV/Å, respectively. Gamma-centered Monkhorst-Pack *k*-point grid sampling was used for the Brillouin zone with density of at least 1000/(the number of atoms per cell) in all geometry optimization and self-consistent calculations. To account for the strong correlation of transition-metal d-electrons, PBE + U method was used in the calculations to correctly characterize the localization properties, with the Hubbard U parameters for Ti set as 4.2 eV. DFT-D3 semi-empirical van der Waals correction was applied to deal with the dispersion force during geometry optimization.

The oxygen vacancy formation energies were calculated using the following formula:

$$E_{vac} = E(\text{vacancy}) - E(\text{perfect}) + 1/2E(O_2)$$

$E(O_2)$ is the total energy of oxygen molecule, and $E$(vacancy) and $E$(perfect) are the total energies of structures with and without oxygen vacancy, respectively. An energy correction of −1.36 eV for the $O_2$ molecule was used in calculations to correct for the self-interaction errors within GGA functional.

The voltage plateaus were calculated using the following formula:

$$U = -\frac{E(\text{perfect}) - nE(\text{Li}) - E(\text{vacancy})}{n}$$

$E$(Li) is the total energy of Li atom in Li metal, and $E$(vacancy) and $E$(perfect) are the total energies of structures with and without lithium vacancy, respectively.

## CRediT authorship contribution statement

**Jianjun Fang:** Formal analysis, Data curation, Conceptualization. **Kunchen Xie:** Formal analysis, Data curation, Conceptualization. **Yongli Song:** Formal analysis, Data curation, Conceptualization. **Kangyi Zhang:** Formal analysis, Data curation. **Fei Xu:** Formal analysis, Data curation. **Xiaoze Shi:** Formal analysis, Data curation. **Ming Ren:** Formal analysis, Data curation. **Minzhi Zhan:** Conceptualization. **Hai Lin:** Formal analysis, Data curation. **Luyi Yang:** Writing – original draft, Data curation, Conceptualization. **Shunning Li:** Writing – review & editing, Writing – original draft, Formal analysis, Data curation, Conceptualization. **Feng Pan:** Writing – review & editing, Writing – original draft, Funding acquisition, Formal analysis, Data curation, Conceptualization.

## Declaration of competing interest

The authors declare no conflict of interests.

## Acknowledgements

This work was financially supported by the National Natural Science Foundation of China (No. 52102200); the Major Science and Technology Infrastructure Project of Material Genome Big-science Facilities Platform supported by Municipal Development and Reform Commission of Shenzhen, Basic and Applied Basic Research Foundation of Guangdong Province (No. 2021B1515130002); International Joint Research Center for Electric Vehicle Power Battery and Materials (No. 2015B01015); Guangdong Key Laboratory of Design and Calculation of New Energy Materials (No. 2017B030301013).

## Appendix A. Supplementary data

Supplementary data to this article can be found online at https://doi.org/10.1016/j.cjsc.2024.100504.

## References


[1] J. Li, J. Fleetwood, W.B. Hawley, W. Kays, From materials to cell: state-of-the-art and prospective technologies for lithium-ion battery electrode processing, Chem. Rev. 122 (2022) 903–956.

[2] H. Adenusi, G.A. Chass, S. Passerini, K.V. Tian, G.H. Chen, Lithium batteries and the solid electrolyte interphase (SEI)-progress and outlook, Adv. Energy Mater. 13 (2023) 2203307.

[3] M.S. Balogun, W. Qiu, Y. Luo, H. Meng, W. Mai, A. Onasanya, T.K. Olaniyi, Y. Tong, A review of the development of full cell lithium-ion batteries: the impact of nanostructured anode materials, Nano Res. 9 (2016) 2823–2851.

[4] C.Y. Wang, T. Liu, X.G. Yang, S.H. Ge, N.V. Stanley, E.S. Rountree, Y.J. Leng, B.D. McCarthy, Fast charging of energy-dense lithium-ion batteries, Nature 611 (2022) 485–490.

[5] D. Song, Z. Yang, Q. Zhao, X. Sun, Y. Wu, Y. Zhang, J. Gao, C. Wang, L. Yang, T. Ohsaka, F. Matsumoto, J. Wu, Dilute electrolyte to mitigate capacity decay and voltage fading of Co-free Li-rich cathode for next-generation Li-ion batteries, ACS Appl. Mater. Interfaces 14 (2022) 12264–12275.

[6] C.Y. Du, Z.Y. Zhao, H. Liu, F.Y. Song, L.L. Chen, Y. Cheng, Z.H. Guo, The status of representative anode materials for lithium-ion batteries, Chem. Rec. 23 (2023) e202300004.

[7] X. Zhang, J. Chen, Z. Xu, Q. Dong, H. Ao, Z. Hou, Y. Qian, Aqueous electrolyte with moderate concentration enables high-energy aqueous rechargeable lithium ion battery for large scale energy storage, Energy Storage Mater. 46 (2022) 147–154.

[8] B. Zhao, R. Ran, M. Liu, Z. Shao, A comprehensive review of $Li_4Ti_5O_{12}$-based electrodes for lithium-ion batteries: the latest advancements and future perspectives, Mater. Sci. Eng. R Rep. 98 (2015) 1–71.

[9] Y.H. Zhang, Z.H. Nie, C.Q. Du, J.W. Zhang, J.W. Zhang, Ultrahigh lithiation dynamics of $Li_4Ti_5O_{12}$ as an anode material with open diffusion channels induced by chemical presodiation, Rare Met. 42 (2023) 471–483.

[10] C. Wang, S.A. Wang, Y.B. He, L.K. Tang, C.P. Han, C. Yang, M. Wagemaker, B.H. Li, Q.H. Yang, J.K. Kim, F.Y. Kang, Combining fast Li-ion battery cycling with large volumetric energy density: grain boundary induced high electronic and ionic conductivity in $Li_4Ti_5O_{12}$ spheres of densely packed nanocrystallites, Chem. Mater. 27 (2015) 5647–5656.

[11] Z. Chen, H. Li, L. Wu, X. Lu, X. Zhang, $Li_4Ti_5O_{12}$ anode: structural design from material to electrode and the construction of energy storage devices, Chem. Rec. 18 (2018) 350–380.

[12] J. Xu, X. Ji, J. Zhang, C. Yang, P. Wang, S. Liu, K. Ludwig, F. Chen, P. Kofinas, C. Wang, Aqueous electrolyte design for super-stable 2.5 V $LiMn_2O_4||Li_4Ti_5O_{12}$ pouch cells, Nat. Energy 7 (2022) 186–193.

[13] T. Yuan, Z.P. Tan, C.R. Ma, J.H. Yang, Z.F. Ma, S.Y. Zheng, Challenges of spinel $Li_4Ti_5O_{12}$ for lithium-ion battery industrial applications, Adv. Energy Mater. 7 (2017) 1601625.

[14] K. Wen, X. Tan, T. Chen, S. Chen, S. Zhang, Fast Li-ion transport and uniform Li-ion flux enabled by a double-layered polymer electrolyte for high performance Li metal battery, Energy Storage Mater. 32 (2020) 55–64.

[15] K.H. Wen, X. Tan, T.H. Chen, S.M. Chen, S.J. Zhang, Fast Li-ion transport and uniform Li-ion flux enabled by a double-layered polymer electrolyte for high performance Li metal battery, Energy Storage Mater. 32 (2020) 55–64.

[16] S.F. Huang, Y. Lv, D. Tie, Y. Yu, Y.F. Zhao, Realizing simultaneously enhanced energy and power density full-cell construction using mixed hard carbon/$Li_4Ti_5O_{12}$ electrode, Rare Met 40 (2019) 65–71, https://doi.org/10.1007/s12598-019-01312-4.

[17] L. Zhao, Y.S. Hu, H. Li, Z. Wang, L. Chen, Porous $Li_4Ti_5O_{12}$ coated with N-doped carbon from ionic liquids for Li-ion batteries, Adv. Mater. 23 (2011) 1385–1388.

[18] T.F. Yi, S.Y. Yang, X.Y. Li, J.H. Yao, Y.R. Zhu, R.S. Zhu, Sub-micrometric $Li_{4-x}Na_xTi_5O_{12}$ ($0 \le x \le 0.2$) spinel as anode material exhibiting high rate capability, J. Power Sources 246 (2014) 505–511.

[19] B. Li, C. Han, Y.B. He, C. Yang, H. Du, Q.H. Yang, F. Kang, Facile synthesis of $Li_4Ti_5O_{12}$/C composite with super rate performance, Energy Environ. Sci. 5 (2012) 9595–9602.

[20] Z.Y. Pu, Q.Y. Lan, Y.M. Li, S.M. Liu, D.L. Yu, X.J. Lv, Preparation of W-doped hierarchical porous $Li_4Ti_5O_{12}$/brookite nanocomposites for high rate lithium ion batteries at –20 °C, J. Power Sources 437 (2019) 226890.

[21] D. Capsoni, M. Bini, V. Massarotti, P. Mustarelli, S. Ferrari, G. Chiodelli, M.C. Mozzati, P. Galinetto, Cr and Ni doping of $Li_4Ti_5O_{12}$: cation distribution and functional properties, J. Phys. Chem. C 113 (2009) 19664–19671.

[22] K. Liang, H. He, Y. Ren, J. Luan, H. Wang, Y. Ren, X. Huang, $Ti^{3+}$ self-doped $Li_4Ti_5O_{12}$ with rich oxygen vacancies for advanced lithium-ion batteries, Ionics 26 (2020) 1739–1747.

[23] X. Zhou, T. Pu, G. Yang, W. Ma, B. Yang, Y. Dai, Origin and effect of oxygen defect in $Li_4Ti_5O_{12}$ prepared with carbon source, J. Electrochem. Soc. 166 (2019) A448–A454.

[24] Y. Zhou, S. Xiao, Z. Li, X. Li, J. Liu, R. Wu, J. Chen, Introducing oxygen vacancies in $Li_4Ti_5O_{12}$ via hydrogen reduction for high-power lithium-ion batteries, Processes 9 (2021) 1655.

[25] Q. Guo, X. Cheng, Y. Shi, Z. Sheng, C. Chang, Bluish $Li_4Ti_5O_{12}$ with enhanced rate performance, J. Alloys Compd. 710 (2017) 383–392.

[26] X. Ma, D. Feng, Y. Xiao, Y. Qian, Q. Wang, Y. Kang, D. Xu, H. Zhao, H. Xu, H. Yi, J. Zheng, J. Wang, C. Wang, Y. Deng, Generating lithium fluoride-abundant interphase on layered lithium-rich oxide cathode with lithium 1,1,2,2,3,3-hexafluoropropane-1,3-disulfonimide, J. Power Sources 507 (2021) 230278.

[27] Y. Liu, R. Xiao, Y. Fang, P. Zhang, Three-dimensional oxygen-deficient $Li_4Ti_5O_{12}$ nanospheres as high-performance anode for lithium ion batteries, Electrochim. Acta 211 (2016) 1041–1047.

[28] T. Sekiya, K. Ichimura, M. Igarashi, S. Kurita, Absorption spectra of anatase $TiO_2$ single crystals heat-treated under oxygen atmosphere, J. Phys. Chem. Solid. 61 (2000) 1237–1242.

[29] J. Chen, N.A. Bogdanov, D. Usvyat, W. Fang, A. Michaelides, A. Alavi, The color center singlet state of oxygen vacancies in $TiO_2$, J. Chem. Phys. 153 (2020) 204704.

[30] M. Michalska, J. Pavlovsky, P. Peikertova, S. Holesova, K.S. Anuratha, J.Y. Lin, Mesoporous/Microporous $Li_4Ti_5O_{12}$/rutile-$TiO_2$ as an anode material for lithium-ion batteries synthesized by the sol-gel method, Solid State Ionics 384 (2022) 116005.

[31] G.Y. Liu, H.Y. Wang, G.Q. Liu, Z.Z. Yang, B. Jin, Q.C. Jiang, Synthesis and electrochemical performance of high-rate dual-phase $Li_4Ti_5O_{12}$–$TiO_2$ nanocrystallines for Li-ion batteries, Electrochim. Acta 87 (2013) 218–223.

[32] X. Zheng, X. Wang, X. Cai, L. Xing, M. Xu, Y. Liao, X. Li, W. Li, Constructing a protective interface film on layered lithium-rich cathode using an electrolyte additive with special molecule structure, ACS Appl. Mater. Interfaces 8 (2016) 30116–30125.

[33] Y. Song, X. Wang, L.L. Tao, B. Song, L. Zhang, Y. Zhang, Y. Sui, Z. Liu, J. Tang, X.F. Han, Effect of Ga-doping and oxygen vacancies on the ferromagnetism of $TiO_2$ thin films, J. Alloys Compd. 694 (2017) 929–934.

[34] Y. Song, L. Yang, J. Li, M. Zhang, Y. Wang, S. Li, S. Chen, K. Yang, K. Xu, F. Pan, Synergistic dissociation-and-trapping effect to promote Li-ion conduction in polymer electrolytes via oxygen vacancies, Small 17 (2021) 2102039.

[35] J. Wang, H. Zhao, Z. Li, Y. Wen, Q. Xia, Y. Zhang, G. Yushin, Revealing rate limitations in nanocrystalline $Li_4Ti_5O_{12}$ anodes for high-power lithium ion batteries, Adv. Mater. Interfaces 3 (2016) 1600003.

[36] Y. Zhang, P. Chen, Q. Wang, Q. Wang, K. Zhu, K. Ye, G. Wang, D. Cao, J. Yan, Q. Zhang, High-capacity and kinetically accelerated lithium storage in $MoO_3$ enabled by oxygen vacancies and heterostructure, Adv. Energy Mater. 11 (2021) 2101712.

[37] S. Ganapathy, M. Wagemaker, Nanosize storage properties in spinel $Li_4Ti_5O_{12}$ explained by anisotropic surface lithium insertion, ACS Nano 6 (2012) 8702–8712.

[38] W.J.H. Borghols, M. Wagemaker, U. Lafont, E.M. Kelder, F.M. Mulder, Size effects in the $Li_4Ti_5O_{12}$ spinel, J. Am. Chem. Soc. 131 (2009) 17786–17792.

[39] Z. Su, S.N. Li, L. Ma, T.C. Liu, M. Li, T.P. Wu, Q.H. Zhang, C. Dong, C. Lai, L. Gu, J. Lu, F. Pan, S.Q. Zhang, Quenching-induced defects liberate the latent reversible capacity of lithium titanate anode, Adv. Mater. 35 (2023) 2208573.

[40] M.M. Rahman, J.Z. Wang, M.F. Hassan, D. Wexler, H.K. Liu, Amorphous carbon coated high grain boundary density dual phase $Li_4Ti_5O_{12}$–$TiO_2$: a nanocomposite anode material for li-ion batteries, Adv. Energy Mater. 1 (2011) 212–220.

[41] Z.D. Li, Y.C. Zhang, H.F. Xiang, X.H. Ma, Q.F. Yuan, Q.S. Wang, C.H. Chen, Trimethyl phosphite as an electrolyte additive for high-voltage lithium-ion batteries using lithium-rich layered oxide cathode, J. Power Sources 240 (2013) 471–475.

[42] C. Wang, S. Wang, Y.B. He, L. Tang, C. Han, C. Yang, M. Wagemaker, B. Li, Q.H. Yang, J.K. Kim, F. Kang, Combining fast Li-ion battery cycling with large volumetric energy density: grain boundary induced high electronic and ionic conductivity in $Li_4Ti_5O_{12}$ spheres of densely packed nanocrystallites, Chem. Mater. 27 (2015) 5647–5656.

[43] L.F. Shen, X.G. Zhang, E. Uchaker, C.Z. Yuan, G. Cao, $Li_4Ti_5O_{12}$ nanoparticles embedded in a mesoporous carbon matrix as a superior anode material for high rate lithium ion batteries, Adv. Energy Mater. 2 (2012) 691–698.

[44] Q.Y. Zhang, H.S. Lu, H.X. Zhong, X.D. Yan, C.Y. Ouyang, L.Z. Zhang, $W^{6+}$ & $Br^-$ codoped $Li_4Ti_5O_{12}$ anode with super rate performance for Li-ion batteries, J. Mater. Chem. A 3 (2015) 13706–13716.

[45] J. Kim, K.E. Lee, K.H. Kim, S. Wi, S. Lee, S. Nam, C. Kim, S.O. Kim, B. Park, Single-layer graphene-wrapped $Li_4Ti_5O_{12}$ anode with superior lithium storage capability, Carbon 114 (2017) 275–283.

[46] Q. Wang, H. Li, R. Zhang, Z. Liu, H. Deng, W. Cen, Y. Yan, Y. Chen, Oxygen vacancies boosted fast $Mg^{2+}$ migration in solids at room temperature, Energy Storage Mater. 51 (2022) 630–637.

[47] C.A. Zhou, K. Ma, Z. Zhuang, M. Ran, G. Shu, C. Wang, L. Song, L. Zheng, H. Yue, D. Wang, Tuning the local environment of Pt species at CNT@$MO_{2-x}$ (M = Sn and Ce) heterointerfaces for boosted alkaline hydrogen evolution, J. Am. Chem. Soc. 146 (2024) 21453–21465.

[48] X. Hou, M. Ruan, L. Zhou, J. Wu, B. Meng, W. Huang, K. Zhong, K. Yang, Z. Fang, K. Xie, Superior lithium storage performance in $MoO_3$ by synergistic effects: oxygen vacancies and nanostructures, J. Energy Chem. 78 (2023) 91–101.

[49] Z. Chen, L. Xu, Q. Chen, P. Hu, Z. Liu, Q. Yu, T. Zhu, H. Liu, G. Hu, Z. Zhu, L. Zhou, L. Mai, Spray-pyrolysis-assisted synthesis of yolk@shell anatase with rich oxygen vacancies for efficient sodium storage, J. Mater. Chem. A 7 (2019) 6740–6746.

[50] P.F. Xiao, M.O. Lai, L. Lu, Transport and electrochemical properties of high potential tavorite $LiVPO_4F$, Solid State Ion. 242 (2013) 10–19.

[51] Y. Xu, M. Zhou, C. Zhang, C. Wang, L. Liang, Y. Fang, M. Wu, L. Cheng, Y. Lei, Oxygen vacancies: effective strategy to boost sodium storage of amorphous electrode materials, Nano Energy 38 (2017) 304–312.

[52] Z. Hong, K. Zhou, Z. Huang, M. Wei, Iso-oriented anatase $TiO_2$ mesocages as a high performance anode material for sodium-ion storage, Sci. Rep. 5 (2015) 11960.